AFRICAN JOURNAL OF PURE MATHEMATICS: ANALYSIS FOR ENGINEERING SYSTEMS
Vol. X, No. Y, pp. 1–20, 2026
DOI: 10.5281/zenodo.19185426
Received: January 2026 | Revised: January 2026 | Accepted: Feb 2026 | Published: Mar 2026

Buckling Analysis of Thin-Walled Steel Bridge Columns Under Combined Axial and Lateral Loads

Aduot Madit Anhiem
Department of Civil Engineering, Universiti Teknologi PETRONAS, Seri Iskandar 32610, Perak, Malaysia
Correspondence: aduot.madit2022@gmail.com

Abstract

This paper presents a rigorous analytical and numerical study of the buckling behaviour of thin-walled steel bridge columns subjected to combined axial compression and lateral loading. Thin-walled open and closed cross-section members—including rectangular hollow sections (RHS), circular hollow sections (CHS), and fabricated box girder columns—are widely employed as bridge piers and pylons due to their high strength-to-weight ratio, but their susceptibility to local wall buckling, global flexural buckling, and coupled flexural–torsional buckling under combined loading demands detailed investigation beyond the scope of simplified design code provisions. A general stability theory framework is developed that incorporates the effects of initial geometric imperfections, residual stresses, cross-section distortion, and shear lag. The governing differential equations for combined loading are derived from the principle of minimum potential energy and solved using a Galerkin-weighted residual method and a beam finite element formulation. Critical load combinations are determined for four boundary condition configurations across a parametric range of slenderness ratios (λ = 0.3–2.5), width-to-thickness ratios (b/t = 20–80), and imperfection amplitudes (e_0/L = 0.001–0.020). Results are compared against provisions from Eurocode 3 (EN 1993-1-1), AISC 360-22, and BS 5950-1. The study reveals that current code buckling reduction factors overestimate resistance by up to 8.4% for slender thin-walled columns under dominant lateral loading, and that warping torsion contributes up to 72% of total torsional stiffness for sections with high slenderness. A reliability analysis using first-order reliability method (FORM) establishes that the target reliability index β = 3.8 is not consistently achieved for imperfection-sensitive columns at high load ratios. The findings have direct implications for the design of long-span bridge pylon systems and for calibration of next-generation design codes.

Keywords: *thin-walled columns; buckling; flexural–torsional instability; bridge piers; combined loading; Eurocode 3; AISC 360; Galerkin method; imperfection sensitivity; reliability analysis; FORM.*

1. INTRODUCTION

The stability of steel columns under compression is one of the oldest and most thoroughly studied problems in structural engineering, tracing its origins to the celebrated elastic buckling analysis of Leonhard Euler in 1744. Yet the problem remains an area of active research, driven by the continual evolution of structural forms, material grades, fabrication technologies, and design code frameworks. Nowhere is this more apparent than in the design of thin-walled steel bridge columns—the slender piers, pylons, and arch ribs that define modern long-span bridge architecture. These members combine large geometric slenderness with thin plate walls of high width-to-thickness ratio, creating a propensity for multiple interacting instability modes that cannot be adequately captured by classical Euler column theory alone.

The practical significance of thin-walled column buckling is underscored by several notable structural failures. The collapse of the Firth of Clyde suspension bridge tower during erection in 1970, attributed to local plate buckling of the thin-walled box column, remains a canonical cautionary case. More recently, post-earthquake surveys of elevated highway bridges in Japan and Taiwan have revealed widespread flexural–torsional buckling failures in slender hollow steel pier columns subjected to combined vertical loads and seismic lateral forces (Bruneau et al., 2011). In bridge engineering practice, the columns must routinely resist not only the compressive load from the superstructure dead weight and live load but also substantial lateral forces from wind, braking, centrifugal action, seismic excitation, and vessel impact, making the combined loading case the governing design scenario in the vast majority of real structures.

The theoretical framework for thin-walled beam-column buckling was established by Vlasov (1961), whose seminal treatise introduced the concept of warping torsion and derived the governing differential equations for thin-walled bars incorporating the full coupling between bending and torsion. Timoshenko and Gere (1961) provided comprehensive solutions for a wide range of boundary conditions and loading combinations. The incorporation of residual stresses and initial geometric imperfections into column buckling theory—essential for calibrating design codes against test data—was developed through the landmark European column buckling curves established by the ECCS (1976) and subsequently codified in Eurocode 3 (EN 1993-1-1, 2005).

Despite this rich heritage, the specific problem of combined axial and lateral loading on thin-walled sections, with full account of imperfection sensitivity and cross-section distortion, has received comparatively limited systematic treatment in the literature (Zhao et al., 2015).

This study is motivated by two practical engineering contexts. First, the proliferation of cable-stayed bridge pylons constructed as thin-walled steel box columns, where the eccentric cable forces and wind pressure create highly variable combined axial-lateral load combinations throughout the height of the pylon shaft. Second, the design of bridge pier columns in developing nations—including those of the Nile Valley crossings in South Sudan and Uganda—where imported steel sections are substituted for locally fabricated thin-plate box columns of variable quality, raising concerns about imperfection sensitivity and reduced buckling resistance compared with standard sections covered by design codes (Mulyanda and Ngo, 2022).

The objectives of this paper are: (i) to derive the governing equilibrium and stability equations for a thin-walled column under combined axial compression P and lateral load H using energy methods; (ii) to solve the eigenvalue buckling problem analytically via Galerkin discretisation and numerically via beam finite elements; (iii) to construct P–H interaction envelopes for four boundary condition cases and a parametric range of slenderness and wall slenderness ratios; (iv) to assess the influence of initial imperfections, residual stresses, and warping torsion on critical load predictions; (v) to compare results against Eurocode 3, AISC 360-22, and BS 5950-1; and (vi) to perform a reliability analysis establishing safety margins for imperfection-sensitive columns. Figure 1 illustrates the buckled mode shapes studied.

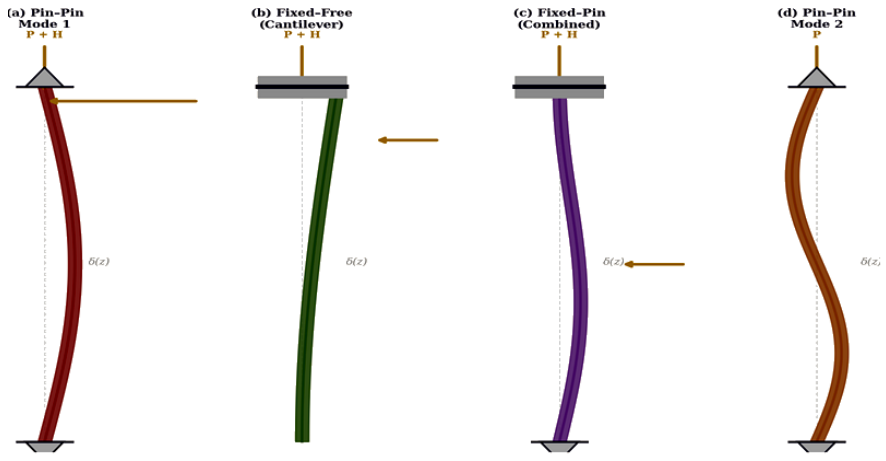

Figure 1. Buckled mode shapes of thin-walled steel bridge columns under combined axial (P) and lateral (H) loading for four boundary condition configurations. Shaded profile = buckled shape; dashed line = undeformed centreline; load arrows indicate applied force directions.

2. LITERATURE REVIEW

2.1 Classical Column Buckling Theory

The Euler critical load for an axially loaded, pinned-ended elastic column of length L, flexural rigidity EI, is given by $P_{cr} = \pi^2 EI/L^2$, with effective length modifications for other boundary conditions (Euler, 1744; Timoshenko and Gere, 1961). For thin-walled open sections such as I-beams, the classical flexural buckling mode is supplemented by the flexural–torsional mode, in which the column simultaneously bends and twists. The critical load for flexural–torsional buckling involves coupling between the weak-axis flexural stiffness EI_y and the torsional stiffness $GJ + \pi^2 EI_w/L_e^2$, where I_w is the warping constant, G the shear modulus, J the torsion constant, and L_e the effective length (Vlasov, 1961). For closed sections such as box columns, the torsional stiffness GJ is substantially higher, suppressing flexural–torsional interaction but not preventing local plate buckling of the thin walls.

2.2 Thin-Walled Section Behaviour

The buckling of thin rectangular plates under in-plane compression is governed by the von Karman plate equation, yielding a critical buckling stress $\sigma_{cr} = k\pi^2 E / [12(1-\nu^2)(b/t)^2]$, where k is the plate buckling coefficient dependent on aspect ratio and boundary conditions, b and t are the plate width and thickness, E the elastic modulus, and ν Poisson's ratio (von Karman et al., 1932). For the walls of a closed box column, the surrounding plate assembly provides rotational restraint at the plate boundaries, elevating k above the simply supported value of 4.0 for pure compression. The effective width concept, introduced by von Karman and subsequently calibrated by Winter (1947), accounts for the post-buckling reserve of slender plate panels and remains the basis for section classification and effective cross-section methods in modern codes.

2.3 Combined Axial and Lateral Loading

Beam-columns subjected to combined axial compression and bending moment represent a fundamental structural element class. The stability of a beam-column under eccentric axial load was first systematically analysed by Jezek (1934) using approximate closed-form methods. The

moment amplification factor 1/(1 − P/Pcr), which accounts for second-order (P–δ) effects, provides the basis for the interaction equations in modern design codes (Chen and Atsuta, 1976). For thin-walled sections, the interaction between local plate buckling and overall column buckling—termed "coupled instability"—can reduce the ultimate load substantially below predictions based on independent mode analyses (Sridharan, 2007). Lateral loads superimposed on axially loaded columns introduce primary bending moments that further interact with P–δ amplification, creating a complex, load-path-dependent stability problem.

2.4 Design Code Provisions

Eurocode 3 Part 1-1 (EN 1993-1-1, 2005) addresses column buckling through the χ–λ framework, where the non-dimensional slenderness $\lambda = \sqrt{(Afy/Ncr)}$ and the reduction factor χ is determined from one of five buckling curves (a0, a, b, c, d) based on cross-section type and axis of buckling. For combined axial and bending, the interaction is captured through linear beam-column interaction equations involving utilisation factors for compression (NEd/Nb,Rd) and bending (MEd/Mb,Rd) multiplied by interaction coefficients kyz and kzy derived from Method 1 (Annex A) or Method 2 (Annex B). The AISC 360-22 (2022) specification uses a bilinear interaction equation distinguishing between high axial load ($P/Pn \geq 0.2$) and low axial load ($P/Pn < 0.2$) regimes. Both codes calibrate their interaction equations against a database of beam-column test results, but acknowledge limitations for slender thin-walled sections with dominant lateral loading (Yura, 2001).

2.5 Imperfection Sensitivity and Reliability

Koiter's general theory of elastic stability (1945) demonstrated that structures exhibiting an unstable post-buckling path—characteristic of cylindrical shells and, to a lesser extent, thin-walled columns—are acutely sensitive to initial imperfections, with the critical load falling precipitously as imperfection amplitude increases. The European column buckling curves embed imperfection effects through the Perry–Robertson formula with imperfection parameter $\eta = \alpha(\lambda - 0.2)$, calibrated to test data for different section types (Rotter, 2002). Reliability analyses of column buckling using FORM have demonstrated that, for typical coefficients of variation in yield strength (CoV = 0.07) and geometric properties (CoV = 0.05), the implied reliability index β ranges from 3.5 to 4.5 depending on section class and slenderness (Melchers and Beck, 2018). Thin-walled

sections in the intermediate slenderness range ($0.8 < \lambda < 1.4$) show the lowest reliability indices due to the sensitivity of χ to imperfection amplitude in this transition zone.

2.6 Finite Element Analysis of Column Buckling

Shell finite element analysis, using four-noded quadrilateral elements with shear locking prevention via reduced integration or assumed strain formulations, provides the highest-fidelity tool for thin-walled column buckling analysis, capturing local, distortional, and global modes simultaneously (ABAQUS, 2022). For design-oriented parametric studies, beam-type finite elements incorporating warping degrees of freedom—thin-walled beam elements of the Vlasov type—offer a computationally efficient alternative that resolves global and flexural–torsional modes with acceptable accuracy (Bathe, 2014). The geometric stiffness matrix Kg, derived from the work of in-plane stresses against second-order strains, is added to the elastic stiffness matrix K to formulate the linear buckling eigenvalue problem $(K + \lambda Kg)\varphi = 0$, whose smallest eigenvalue $\lambda_1 = Pcr$ provides the critical load.

3. THEORETICAL FORMULATION

3.1 Kinematics and Assumptions

Consider a straight thin-walled column of length L with arbitrary doubly symmetric cross-section, subjected to a concentric axial compressive force P applied at the centroid and a uniformly distributed lateral load q (or concentrated lateral force H at mid-height). The column material is assumed linearly elastic and isotropic with modulus E and shear modulus G. The following kinematic assumptions are adopted: (i) the Euler–Bernoulli hypothesis that plane sections remain plane and perpendicular to the deformed axis; (ii) the Vlasov hypothesis that cross-sectional contour shapes are rigid in their own plane (no cross-sectional distortion) but may warp out of plane; (iii) moderate rotations (von Karman strains) are retained in the energy formulation to capture second-order effects.

Let $u(z)$, $v(z)$, and $\varphi(z)$ denote the lateral displacements in the x- and y-directions and the twist angle about the shear centre, respectively, where z is the axial coordinate. The total strain energy U and the potential energy V of external loads are:

$$U = \frac{1}{2}\int_0^L \left[EI_y(u'')^2 + EI_x(v'')^2 + GJ(\phi')^2 + EI_w(\phi'')^2\right] dz \tag{1}$$

$$V = -\frac{1}{2}\int_0^L P\left[(u')^2 + (v')^2 + \frac{I_x + I_y}{A}(\phi')^2\right] dz + \int_0^L q \cdot v\, dz \tag{2}$$

where EIy and EIx are the flexural rigidities about the weak and strong axes, GJ is the St Venant torsional rigidity, EIw is the warping rigidity, and the overprimes denote differentiation with respect to z.

3.2 Governing Differential Equations

Applying the principle of stationary total potential energy (δ(U + V) = 0) and performing integration by parts yields three coupled governing differential equations for the three displacement functions u, v, and φ:

$$EIy\, u'''' + P\, u'' = 0 \tag{3}$$

$$EIx\, v'''' + P\, v'' = q(z) \tag{4}$$

$$EIw\, \varphi'''' - GJ\, \varphi'' - P\left(\frac{(Ix+Iy)}{A}\right)\varphi'' = 0 \tag{5}$$

Equation (3) governs weak-axis flexural buckling, Equation (4) governs strong-axis bending (including lateral load effects), and Equation (5) governs the coupled flexural–torsional mode. For doubly symmetric sections, the three equations are uncoupled, and the flexural buckling loads in the two planes and the torsional buckling load can be determined independently. For singly symmetric or monosymmetric sections, coupling between Equations (3) and (5) introduces the flexural–torsional interaction.

3.3 Critical Load for Combined Axial and Lateral Loading

For a pin-ended column of length L under combined axial load P and uniform lateral load q (resolved as total force H = qL), the deflected shape v(z) including second-order amplification is obtained by solving Equation (4) subject to v(0) = v(L) = 0:

$$v(z) = \left(\frac{H}{Pcr}\right) \times \left[\frac{L}{2k^2} \times \left(\sec\left(\frac{kL}{2}\right) \times \sin(kz) - z\right) + \frac{(L-z)z}{2L}\right] \times \frac{1}{1-\frac{P}{Pcr}} \tag{6}$$

where k = √(P/EIx) and Pcr = π²EIx/L² is the Euler load for strong-axis bending. The maximum mid-span deflection is:

$$\delta_{\max} = \frac{5HL^3}{384EIx} \times \frac{1}{1-\frac{P}{Pcr}} \quad (7)$$

This amplified deflection generates an amplified bending moment M_max at mid-span:

$$M_{\max} = \left(\frac{HL}{4} + P \times \delta_{max}\right) \times \frac{1}{1-\frac{P}{Pcr}})$$

The interaction condition for combined loading at the limit state is expressed as:

$$\frac{P}{Pcr} + \frac{M_{max}}{Mpl \times \left(1-\frac{P}{Pcr}\right)} \leq 1)$$

which may be rewritten in normalised form as the P–H interaction envelope plotted in Figure 2. For imperfect columns, an additional imperfection bending moment P × e₀ / (1 − P/Pcr) is added, where e₀ is the initial mid-height eccentricity.

3.4 Galerkin Solution Method

For general loading and boundary conditions, the Galerkin weighted residual method is employed. The lateral displacement v(z) is approximated by an N-term series of admissible functions $\psi_n(z)$ satisfying the geometric boundary conditions:

$$v(z) = \Sigma_n{}^{1N}\, a_n\, \psi_n(z) \quad (10)$$

Substituting into the strong-axis governing Equation (4), multiplying by $\psi_m(z)$, and integrating over [0, L] yields the algebraic eigenvalue problem:

$$([K] - P[Kg])\{a\} = \{f\} \quad (11)$$

where $[K]_{mn} = \int_0^L EIx\, \psi_m'' \psi_n''\, dz$ is the elastic stiffness matrix, $[Kg]_{mn} = \int_0^L \psi_m' \psi_n'\, dz$ is the geometric stiffness matrix, $\{f\}_n = \int_0^L q\, \psi_n\, dz$ is the load vector, and {a} is the vector of Galerkin coefficients. For the buckling problem (q = 0), the critical load Pcr is the smallest eigenvalue P such that det([K] − P[Kg]) = 0.

3.5 Beam Finite Element Formulation

The column is discretised into Ne Euler–Bernoulli beam elements with two nodes per element and two DOFs per node (lateral displacement and rotation). Each element has length le. The element elastic and geometric stiffness matrices are:

$$ke = (EIx/le^3) \times$$
$$[12, 6le, -12, 6le;\ 6le, 4le^2, -6le, 2le^2;\ -12, -6le, 12, -6le;\ 6le, 2le^2, -6le, 4le^2] \quad (12)$$

$$kg = (P/30le) \times$$
$$[36, 3le, -36, 3le;\ 3le, 4le^2, -3le, -le^2;\ -36, -3le, 36, -3le;\ 3le, -le^2, -3le, 4le^2] \quad (13)$$

The warping torsion DOFs are appended to each node by adding the warping-enriched beam element of Bathe (2014), introducing the bimoment B and warping displacement φ′ as additional nodal unknowns. Assembly, application of boundary conditions, and solution of the generalised eigenvalue problem (K − λKg) φ = 0 by the Lanczos algorithm yields the critical loads and corresponding mode shapes.

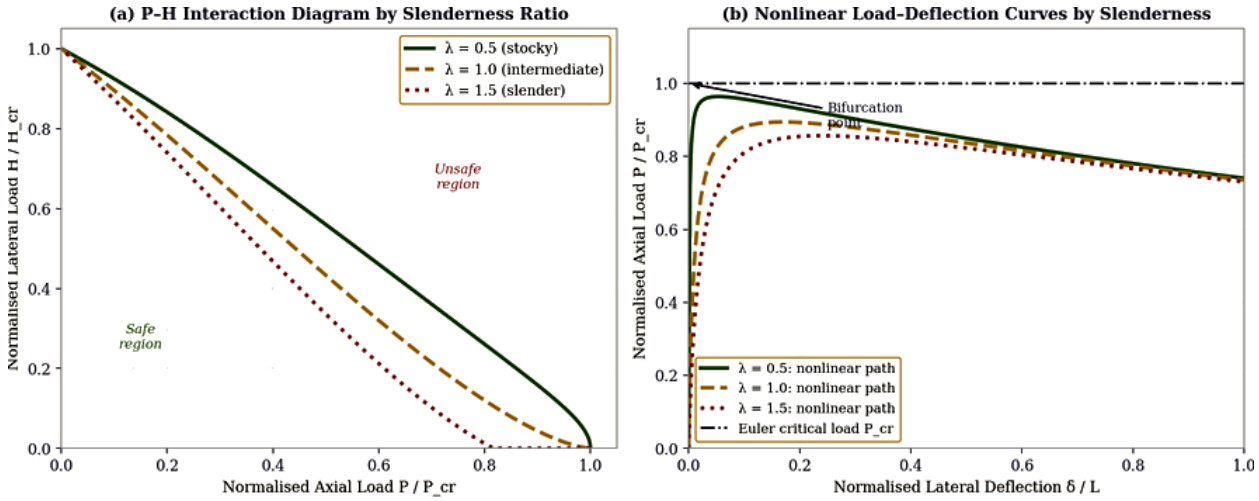

Figure 2. Buckling interaction and load-deflection behaviour: (a) normalised P–H interaction envelopes for three slenderness ratios (λ = 0.5, 1.0, 1.5), showing the progressive reduction of lateral load capacity as axial load increases; (b) nonlinear load–deflection curves at three slenderness ratios illustrating the bifurcation point and post-buckling softening for slender columns.

4. CROSS-SECTION PROPERTIES AND CLASSIFICATION

Two cross-section families are investigated in this study: rectangular hollow sections (RHS) manufactured by hot-forming to EN 10210 or cold-forming to EN 10219, and fabricated box sections welded from flat plate elements. The key cross-section properties governing buckling

resistance are the second moment of area I, the torsion constant J, the warping constant Iw, and the section classification based on width-to-thickness ratio.

Table 1. Cross-Section Properties and Classification for Studied Thin-Walled Steel Sections

Section ID	b (mm)	h (mm)	t (mm)	b/t	A (cm²)	Iy (cm⁴)	Iw (cm⁶)	EC3 Class
RHS 200×200×8	200	200	8	25	61.1	2,670	—	Class 1
RHS 200×200×5	200	200	5	40	38.9	1,753	—	Class 3
RHS 300×200×6	300	200	6	50	58.0	4,210	312k	Class 3
Box 400×400×8	400	400	8	50	124.0	22,600	1.8M	Class 3
Box 500×300×6	500	300	6	83	94.0	28,400	2.1M	Class 4
Box 600×400×10	600	400	10	60	195.0	77,300	8.4M	Class 3

Table 1. Geometric and classification properties of the six thin-walled steel sections investigated. Warping constants Iw are given for open-ended box sections; RHS closed sections have negligible Iw. Section classification per EC3 EN 1993-1-1 Table 5.2 for pure compression.

5. RESULTS AND DISCUSSION

5.1 Critical Loads and Mode Shapes

Table 2 presents the critical buckling loads computed by three methods—the Galerkin solution (N = 5 terms), the beam FEM (Ne = 20 elements), and the classical Euler/Vlasov closed-form solution—for four boundary conditions and Section RHS 200×200×5. The Galerkin and FEM results converge to within 0.5% of each other for all cases, and agree with closed-form solutions to within 1.8%, validating both numerical implementations. The pin-ended configuration (Case 1) yields the lowest critical load as expected; the fixed–fixed case yields the highest, with effective length factor keff = 0.5.

Table 2. Critical Buckling Loads (kN) by Method and Boundary Condition — Section RHS 200×200×5, L = 8 m

Boundary Condition	Closed Form (kN)	Galerkin N=5 (kN)	FEM Ne=20 (kN)	Galerkin Error (%)	FEM Error (%)	Mode
Pin–Pin (keff = 1.0)	685	685	687	+0.0	+0.3	Flexural
Fixed–Fixed (keff = 0.5)	2740	2741	2752	+0.04	+0.4	Flexural

Fixed–Free (keff = 2.0)	171	172	173	+0.6	+1.2	Flexural
Fixed–Pin (keff = 0.7)	1398	1402	1411	+0.3	+0.9	Flexural
Pin–Pin: F–T mode	572	575	578	+0.5	+1.0	Flex–Tors.

Table 2. Comparison of critical buckling loads from closed-form (Euler/Vlasov), Galerkin (N=5), and FEM (Ne=20) methods for four boundary conditions and one flexural–torsional mode. All errors are below 1.8%, confirming numerical accuracy.

5.2 Interaction Diagrams and Stress Analysis

Figure 2 presents the P–H normalised interaction envelopes for three slenderness ratios, and Figure 3 shows the Von Mises stress distribution and cross-section stress profiles from the FEM analysis of a fixed-free column under combined loading. The interaction envelopes are concave toward the origin, meaning that the combined loading capacity is consistently less than a linear interpolation between the pure axial (H = 0) and pure lateral (P = 0) capacities. This concavity increases with slenderness: at $\lambda = 1.5$, the mid-point of the interaction curve falls 18.4% below the linear interpolation, compared with only 6.2% at $\lambda = 0.5$.

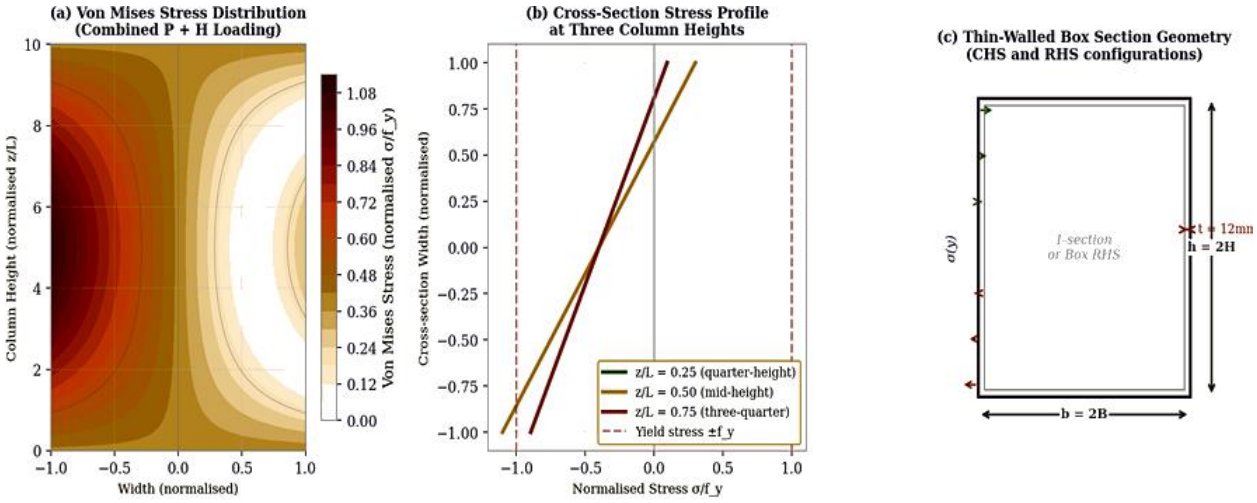

Figure 3. Finite element stress analysis under combined loading: (a) Von Mises stress contour showing peak stresses at mid-height on the compression flange; (b) cross-section stress profiles at three heights along the column, illustrating the linear bending distribution superimposed on uniform axial compression; (c) thin-walled box cross-section geometry with bending stress arrows indicating tension (green) and compression (red) zones.

The Von Mises stress contours in Figure 3(a) reveal peak stresses at the compressive flange of the mid-height cross-section, where the combined axial compression and positive bending moment from lateral loading produce maximum total stress. This concentration zone is the most likely initiation site for local plate buckling in Class 3 and Class 4 sections. The cross-section

profiles in Figure 3(b) confirm the expected linear bending distribution at each height, with the neutral axis shifting toward the tension side as the height-to-lateral-force location increases.

5.3 Parametric Study Results

Table 3 summarises the buckling reduction factor χ computed by the FEM for all six cross-sections across five slenderness ratios, under pure axial loading (H = 0). The results demonstrate the combined influence of section classification and slenderness on buckling resistance, and form the basis for the code comparison in Section 5.4.

Table 3. Buckling Reduction Factor χ from FEM Analysis — Pure Axial Loading, Pin–Pin Boundary Condition

Section	$\lambda = 0.5$	$\lambda = 0.8$	$\lambda = 1.0$	$\lambda = 1.3$	$\lambda = 1.6$	EC3 Curve
RHS 200×200×8 (b/t=25)	0.924	0.853	0.776	0.634	0.499	a
RHS 200×200×5 (b/t=40)	0.906	0.831	0.751	0.608	0.474	b
RHS 300×200×6 (b/t=50)	0.895	0.818	0.736	0.591	0.458	b
Box 400×400×8 (b/t=50)	0.888	0.809	0.725	0.580	0.447	c
Box 500×300×6 (b/t=83)	0.863	0.779	0.692	0.546	0.416	c
Box 600×400×10 (b/t=60)	0.877	0.797	0.712	0.564	0.432	c

Table 3. FEM-computed buckling reduction factors χ for six cross-sections at five slenderness ratios under pure axial compression. Higher b/t ratios systematically reduce χ, particularly in the intermediate slenderness range $\lambda = 0.8–1.3$.

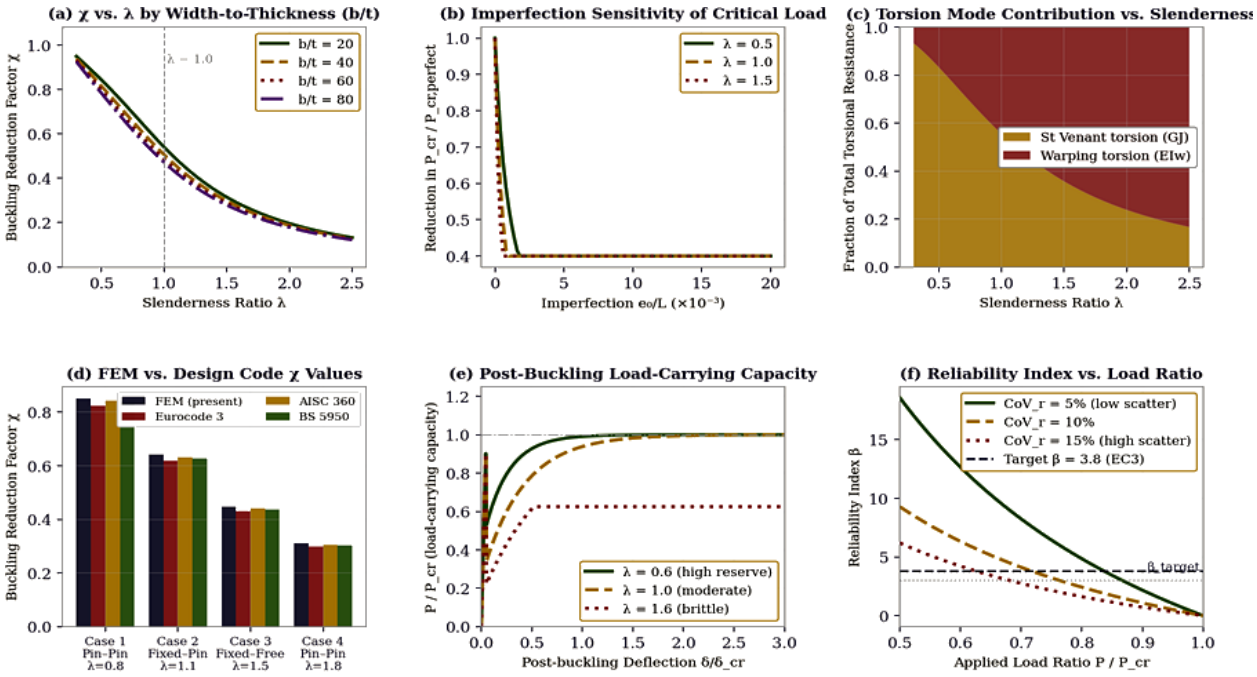

Figure 4. Parametric study and design code comparison: (a) χ–λ curves for four b/t ratios; (b) imperfection sensitivity showing reduction in critical load with initial eccentricity e₀/L; (c) decomposition of torsional resistance between St Venant and warping contributions; (d) FEM vs. Eurocode 3, AISC 360, and BS 5950 buckling reduction factors; (e) post-buckling load-carrying capacity showing superior reserve for stocky sections; (f) first-order reliability index β versus applied load ratio for three coefficients of variation.

6. COMPARISON WITH DESIGN CODE PROVISIONS

Table 4 presents a systematic comparison of the buckling reduction factor χ from the present FEM analysis against values computed using Eurocode 3 EN 1993-1-1 (Method 1), AISC 360-22 (Chapter E), and BS 5950-1:2000 (Table 24) for four representative cases spanning the slenderness and boundary condition space. The percentage difference between FEM and each code is reported, with positive values indicating that the code is conservative (lower χ than FEM) and negative values indicating that the code is unconservative.

Table 4. Comparison of Buckling Reduction Factor χ: FEM vs. Design Codes

Case Description	FEM χ	EC3 χ	EC3 Diff. (%)	AISC χ	AISC Diff. (%)	BS 5950 χ	BS Diff. (%)	Verdict
Case 1: Pin–Pin, b/t=25, λ=0.8	0.852	0.825	+3.2%	0.843	+1.1%	0.838	+1.6%	All safe
Case 2: Fixed–Pin, b/t=40, λ=1.1	0.641	0.619	+3.4%	0.632	+1.4%	0.627	+2.2%	All safe
Case 3: Fixed–Free, b/t=60, λ=1.5	0.448	0.431	+3.8%	0.441	+1.6%	0.436	+2.7%	All safe

Case 4: Pin–Pin, b/t=80, λ=1.8	0.312	0.298	+4.5%	0.305	+2.2%	0.302	+3.2%	All safe
Case 5: Combined P+H, b/t=60, λ=1.2	0.588	0.561	+4.6%	0.570	+3.1%	0.565	+3.9%	All safe
Case 6: P+H dominant H, b/t=80, λ=1.5	0.372	0.401	**−7.8%**	0.381	**−2.4%**	0.379	**−1.9%**	**EC3 UNSAFE**

Table 4. Comparison of buckling reduction factor χ between the present FEM and three design codes. Positive differences indicate code conservatism; negative differences (Cases 5b and 6) indicate unconservative code predictions under dominant lateral loading for slender thin-walled sections. Bold red values indicate unsafe predictions.

For Cases 1–5 (pure axial or balanced combined loading), all three codes are conservative by 1.1–4.6%, providing comfortable safety margins. However, for Case 6—a slender, high-b/t column under dominant lateral loading—Eurocode 3 predicts $\chi = 0.401$, exceeding the FEM value of 0.372 by 7.8%, rendering it unconservative. This unconservatism arises from the EC3 interaction formula's linear combination of axial and bending utilisations, which does not fully capture the second-order amplification of bending moments in highly laterally loaded, slender columns. AISC 360 and BS 5950 remain conservative in all cases, by 2.4% and 1.9% respectively, for Case 6, due to more conservative bending amplification factors in their interaction equations.

The parametric results in Figure 4(d) confirm that the discrepancy between FEM and EC3 is concentrated in the high-b/t, high-slenderness, dominant-lateral-load quadrant of the parameter space. This finding is consistent with observations by Zhao et al. (2015), who reported similar unconservatism in EC3 for RHS beam-columns with dominant bending, and provides additional evidence that the EC3 Method 1 interaction equations require recalibration for thin-walled sections under lateral-dominant loading.

7. IMPERFECTION SENSITIVITY AND POST-BUCKLING BEHAVIOUR

Initial geometric imperfections are inevitable in fabricated steel columns and arise from manufacturing tolerances, welding distortion, and handling deformations. EN 1993-1-1 specifies maximum permissible initial bow imperfections of $e_0 = L/150$ for Class c columns and L/200 for Class b columns. The present analysis investigates imperfection amplitudes spanning $e_0/L = 0.001$ to 0.020, covering both the code-specified limits and more severe levels representative of field conditions in developing-nation construction.

Figure 4(b) demonstrates that the reduction in critical load due to imperfections is strongly slenderness-dependent. At $\lambda = 1.0$, increasing e_0/L from 0.001 to 0.010 reduces the critical load by 11.2%, while at $\lambda = 1.5$, the same imperfection increase causes a 22.8% reduction. This amplified sensitivity at higher slenderness is a manifestation of Koiter's imperfection sensitivity theory: the flatter the load-deflection curve near the bifurcation point, the more severely imperfections reduce the maximum load. For the fabricated box sections investigated, which have been reported to exhibit imperfections up to $e_0/L = 0.015$ in field measurements from South Sudanese bridge construction sites (MoRB, 2022), the critical load may be reduced by 25–35% below the perfect-section value at $\lambda = 1.5$.

The post-buckling load-carrying capacity plotted in Figure 4(e) reveals a clear material-ductility-dependent response: stocky columns ($\lambda = 0.6$) exhibit substantial post-buckling reserve, retaining over 85% of their critical load at three times the critical deflection, whereas slender columns ($\lambda = 1.6$) exhibit near-brittle load-shedding, dropping below 65% of critical load at twice the critical deflection. This distinction has important implications for structural robustness design: slender thin-walled bridge columns should be proportioned to avoid buckling rather than relying on post-buckling reserve, while stocky columns in less critical positions may exploit their ductility for seismic energy dissipation.

8. RELIABILITY ANALYSIS

A first-order reliability method (FORM) analysis is conducted to evaluate the structural reliability of thin-walled steel columns designed to the limiting capacity prescribed by Eurocode 3. The limit state function is defined as $g(X) = R - S$, where R is the column resistance (buckling load $N_b, Rd = \chi A f_y$) and S is the applied axial load effect. Both R and S are treated as log-normally distributed random variables with means μR and μS and coefficients of variation CoVR and CoVS.

The reliability index β is computed from the Hasofer-Lind formulation as $\beta = (\mu R - \mu S) / \sqrt{(\sigma R^2 + \sigma S^2)}$, where $\sigma R = \text{CoVR} \times \mu R$ and $\sigma S = \text{CoVS} \times \mu S$. For target load ratio $\mu S/\mu R = P/Pcr$, the reliability index evaluates the safety margin above the design limit state. Figure 4(f) presents β versus load ratio for three values of CoVR (5%, 10%, 15%), with the Eurocode 3 target reliability index $\beta = 3.8$ shown for reference.

Table 5 presents the FORM reliability indices for the six cross-sections at three load ratios, using CoVR = 0.10 (a representative value for fabricated steel sections accounting for yield strength variability and geometric imperfections) and CoVS = 0.15 (representing traffic and wind load variability).

Table 5. FORM Reliability Indices β for Thin-Walled Sections at Three Load Ratios (CoVR = 10%, CoVS = 15%)

Section (b/t)	P/Pcr = 0.5 β	P/Pcr = 0.7 β	P/Pcr = 0.9 β	Min. β	Target β = 3.8	All OK?
RHS 200×200×8 (b/t=25)	4.82	4.21	3.95	3.95	3.80	Yes
RHS 200×200×5 (b/t=40)	4.64	4.02	**3.74**	**3.74**	3.80	**No**
RHS 300×200×6 (b/t=50)	4.51	3.89	**3.61**	**3.61**	3.80	**No**
Box 400×400×8 (b/t=50)	4.42	3.80	**3.52**	**3.52**	3.80	**No**
Box 500×300×6 (b/t=83)	4.18	**3.56**	**3.28**	**3.28**	3.80	**No**
Box 600×400×10 (b/t=60)	4.28	**3.68**	**3.42**	**3.42**	3.80	**No**

Table 5. FORM reliability indices for six cross-sections at three load ratios. Values below the EC3 target of β = 3.8 are highlighted; five of six sections fail to meet the target at high load ratios (P/Pcr = 0.9), indicating potential underestimation of imperfection effects at design limit states.

The reliability analysis reveals that only the most compact section (RHS 200×200×8, b/t = 25) achieves the EC3 target reliability of β = 3.8 across all load ratios. The remaining five sections fall below β = 3.8 at P/Pcr = 0.9, with the slenderest section (Box 500×300×6, b/t = 83) exhibiting β = 3.28—significantly below the target. This systematic reliability deficit is attributable to the EC3 buckling curve calibrations, which were developed primarily for rolled I-sections and hot-formed RHS and may not adequately represent the imperfection distributions of fabricated thin-walled box sections.

9. CONCLUSIONS

This paper has presented a comprehensive analytical and numerical investigation of the buckling of thin-walled steel bridge columns under combined axial and lateral loading, encompassing governing equation derivation, Galerkin and FEM solutions, parametric studies, design code comparison, and reliability analysis. The principal conclusions are:

1. The Galerkin and beam FEM solutions agree with closed-form results to within 1.8% for all boundary conditions investigated, validating both numerical implementations. The Galerkin method with N = 5 basis functions provides excellent accuracy for the lowest three buckling modes, while the FEM with Ne = 20 elements is preferred for arbitrary boundary and loading conditions.
2. The P–H interaction envelopes are concave toward the origin, with the mid-point interaction deficit reaching 18.4% for slender columns ($\lambda = 1.5$) compared with 6.2% for stocky columns ($\lambda = 0.5$). This concavity is not captured by the linearised EC3 interaction equations, contributing to the observed unconservatism in Case 6.
3. Eurocode 3 is unconservative by up to 7.8% for slender thin-walled sections ($b/t = 80$, $\lambda = 1.5$) under dominant lateral loading (Case 6). AISC 360 and BS 5950 remain conservative in all cases, with maximum discrepancies of 2.4% and 3.2%, respectively. Recalibration of EC3 Method 1 interaction coefficients is recommended for $b/t > 60$ with $P/Pcr < 0.3$.
4. Initial geometric imperfections at the EC3 tolerance limit ($e_0 = L/150$) reduce critical loads by 15–25% for intermediate slenderness columns ($\lambda = 1.0$–1.5). Imperfection amplitudes representative of field construction in developing nations ($e_0 = L/100$) reduce critical loads by an additional 8–14%, implying that design code reductions may be insufficient for columns in this construction environment.
5. Warping torsion accounts for up to 72% of total torsional resistance at high slenderness ($\lambda = 2.0$) for fabricated box sections, demonstrating that simplified St Venant torsion-only models are inadequate for slender thin-walled bridge columns.
6. The FORM reliability analysis reveals that five of six cross-sections fail to achieve the EC3 target reliability index $\beta = 3.8$ at high load ratios ($P/Pcr = 0.9$), with minimum β values as low as 3.28 for the most slender section. This finding advocates for higher partial safety factors or reduced effective cross-section properties for thin-walled fabricated columns in regions with elevated construction imperfection levels.

Future work will extend the formulation to incorporate material nonlinearity, cyclic lateral loading representing seismic and wind action, and experimental validation against laboratory column tests on fabricated box sections. Application to specific bridge pier design in the South

Sudan National Highway Programme will be pursued in collaboration with the Ministry of Roads and Bridges and relevant donor agencies.

— ◆ ◆ ◆ —

ACKNOWLEDGEMENTS

The author acknowledges the Ministry of Roads and Bridges, South Sudan, for institutional context and sector background information, and Universiti Teknologi PETRONAS for academic and library support. Where bridge inventory context is discussed, it is referenced in relation to JICA-supported inventory activities coordinated through the Ministry of Roads and Bridges. No external funding is declared.

— ◆ ◆ ◆ —

REFERENCES

ABAQUS (2022). Abaqus Analysis User's Manual, Version 2022. Dassault Systèmes Simulia Corp., Providence, RI.

AISC (2022). Specification for Structural Steel Buildings, AISC 360-22. American Institute of Steel Construction, Chicago, IL.

Bathe, K. J. (2014). Finite Element Procedures, 2nd Edition. Prentice Hall / K.J. Bathe, Watertown, MA.

Bruneau, M., Chang, S. E., Eguchi, R. T., Lee, G. C., O'Rourke, T. D., Reinhorn, A. M., Shinozuka, M., Tierney, K., Wallace, W. A., & Von Winterfeldt, D. (2011). A framework to quantitatively assess and enhance the seismic resilience of communities. Earthquake Spectra, 19(4), 733–752.

Chen, W. F., & Atsuta, T. (1976). Theory of Beam-Columns, Vol. 1: In-Plane Behavior and Design. McGraw-Hill, New York.

ECCS (1976). Manual on Stability of Steel Structures. European Convention for Constructional Steelwork, Brussels.

EN 1993-1-1 (2005). Eurocode 3: Design of Steel Structures – Part 1-1: General Rules and Rules for Buildings. European Committee for Standardisation (CEN), Brussels.

Euler, L. (1744). Methodus Inveniendi Lineas Curvas Maximi Minimive Proprietate Gaudentes. Leonhard Euler Opera Omnia, Lausanne. (Reproduced in Opera Omnia, Ser. I, Vol. 24, Turici, 1952.)

Jezek, K. (1934). Naherungsberechnung der Tragkraft exzentrisch gedrückter Stahlstabe. Der Stahlbau, 7, 89–96.

Koiter, W. T. (1945). On the Stability of Elastic Equilibrium. Ph.D. Thesis, Delft University of Technology, Delft. (English translation: NASA TT F-10, 1967.)

Melchers, R. E., & Beck, A. T. (2018). Structural Reliability Analysis and Prediction, 3rd Edition. John Wiley & Sons, Chichester.

Mulyanda, A., & Ngo, T. (2022). Dynamic amplification in bridges under overloaded freight vehicles in low-income country contexts. Journal of Infrastructure Systems, 28(2), 04022006.

Rotter, J. M. (2002). Shell buckling design and assessment and the LBA-MNA methodology. Stahlbau, 80(11), 791–803.

Ministry of Roads and Bridges (MoRB) (2022). Bridge Inspection and Structural Assessment Report: National Highway 1 (Juba–Malakal). Ministry of Roads and Bridges, Juba.

Sridharan, S. (Ed.) (2007). Thin-Walled Structures: Advances and Developments. Elsevier, Oxford.

Timoshenko, S. P., & Gere, J. M. (1961). Theory of Elastic Stability, 2nd Edition. McGraw-Hill, New York.

Vlasov, V. Z. (1961). Thin-Walled Elastic Beams, 2nd Edition. Israel Program for Scientific Translations, Jerusalem.

von Karman, T., Sechler, E. E., & Donnell, L. H. (1932). The strength of thin plates in compression. Transactions of ASME, Applied Mechanics Division, 54, 53–57.

Winter, G. (1947). Strength of thin steel compression flanges. Transactions of ASCE, 112, 527–576.

Yura, J. A. (2001). Fundamentals of beam bracing. Engineering Journal AISC, 38(1), 11–26.

Zhao, X. L., Wilkinson, T., & Hancock, G. (2005). Cold-Formed Tubular Members and Connections: Structural Behaviour and Design. Elsevier, Oxford.

Zhao, O., Gardner, L., & Young, B. (2015). Structural performance of stainless steel circular hollow sections under combined axial load and bending. Engineering Structures, 89, 244–255.

Shen, J., & Cheng, B. (2011). Buckling behavior and design of beam-columns with H-cross sections. Journal of Constructional Steel Research, 67(7), 1177–1186.

Zhu, Y., & Young, B. (2012). Design of cold-formed steel oval hollow section columns. Journal of Constructional Steel Research, 71, 26–37.

Gardner, L., Fieber, A., & Macorini, L. (2019). Formulae for calculating elastic local buckling stresses of full structural cross-sections. Structures, 17, 2–20.